



# **NAVAL POSTGRADUATE SCHOOL**

**MONTEREY, CALIFORNIA**

## **THESIS**

**DIRECT AND REMOTE EFFECTS OF TOPOGRAPHY  
AND ORIENTATION, AND THE DYNAMICS OF  
MESOSCALE EDDIES**

by

Larry T. Gulliver

September 2017

Thesis Advisor:  
Second Reader:

Timour Radko  
Justin M. Brown

**Approved for public release. Distribution is unlimited.**

THIS PAGE INTENTIONALLY LEFT BLANK

<b>REPORT DOCUMENTATION PAGE</b>			<i>Form Approved OMB No. 0704-0188</i>	
Public reporting burden for this collection of information is estimated to average 1 hour per response, including the time for reviewing instruction, searching existing data sources, gathering and maintaining the data needed, and completing and reviewing the collection of information. Send comments regarding this burden estimate or any other aspect of this collection of information, including suggestions for reducing this burden, to Washington headquarters Services, Directorate for Information Operations and Reports, 1215 Jefferson Davis Highway, Suite 1204, Arlington, VA 22202-4302, and to the Office of Management and Budget, Paperwork Reduction Project (0704-0188) Washington, DC 20503.				
<b>1. AGENCY USE ONLY (Leave blank)</b>		<b>2. REPORT DATE</b> September 2017		<b>3. REPORT TYPE AND DATES COVERED</b> Master's thesis
<b>4. TITLE AND SUBTITLE</b> DIRECT AND REMOTE EFFECTS OF TOPOGRAPHY AND ORIENTATION, AND THE DYNAMICS OF MESOSCALE EDDIES			<b>5. FUNDING NUMBERS</b>	
<b>6. AUTHOR(S)</b> Larry T. Gulliver				
<b>7. PERFORMING ORGANIZATION NAME(S) AND ADDRESS(ES)</b> Naval Postgraduate School Monterey, CA 93943-5000			<b>8. PERFORMING ORGANIZATION REPORT NUMBER</b>	
<b>9. SPONSORING / MONITORING AGENCY NAME(S) AND ADDRESS(ES)</b> N/A			<b>10. SPONSORING / MONITORING AGENCY REPORT NUMBER</b>	
<b>11. SUPPLEMENTARY NOTES</b> The views expressed in this thesis are those of the author and do not reflect the official policy or position of the Department of Defense or the U.S. Government. IRB Protocol number ____ N/A ____.				
<b>12a. DISTRIBUTION / AVAILABILITY STATEMENT</b> Approved for public release. Distribution is unlimited.			<b>12b. DISTRIBUTION CODE</b>	
<b>13. ABSTRACT (maximum 200 words)</b> <p>Baroclinic instability in the ocean is a primary cause of mesoscale eddies, which are pockets of water in the scale of 100km that have different density, thermal, and rotational characteristics than their surroundings. First observed in the early 1900s, eddies are thought to be a predominant reason for the heat flux between the equator and the poles in both the ocean and the atmosphere. In attempt to understand this process better, this study uses a series of numerical simulations performed on high performance computing systems. The calculations are based on the Massachusetts Institute of Technology general circulation model, which is used to compare lateral heat transport between different simulations. The specific objectives of this project include</p> <ul style="list-style-type: none"> <li>i) Comparison the direct and remote interactions of shear with topographic slope. The direct scenario is one in which the shear extends throughout the entire ocean depth and is therefore in direct contact with the sea floor, whereas in the remote scenario there is a spatial separation between the shear in the upper half of the basin and the bottom topography,</li> <li>ii) Analysis of the system response to changes in the zonal and meridional seafloor slope and</li> <li>iii), Investigation of the effect of orientation changes in the mean large-scale current on cross-flow fluxes.</li> </ul> <p>The lateral heat transport and diffusivity of these simulations are then compared to our analytic model, known as Growth Rate Balance, which is based on the balance between growth rate (primary) instabilities deduced from linear theory and numerically generated secondary instabilities.</p>				
<b>14. SUBJECT TERMS</b> mesoscale variability, ocean eddies, baroclinic instability, topography, Task Force Ocean, Massachusetts Institute of Technology general circulation model, ocean modelling, Growth Rate Balance			<b>15. NUMBER OF PAGES</b> 59	
			<b>16. PRICE CODE</b>	
<b>17. SECURITY CLASSIFICATION OF REPORT</b> Unclassified	<b>18. SECURITY CLASSIFICATION OF THIS PAGE</b> Unclassified	<b>19. SECURITY CLASSIFICATION OF ABSTRACT</b> Unclassified	<b>20. LIMITATION OF ABSTRACT</b> UU	

THIS PAGE INTENTIONALLY LEFT BLANK

**Approved for public release. Distribution is unlimited.**

**DIRECT AND REMOTE EFFECTS OF TOPOGRAPHY AND ORIENTATION,  
AND THE DYNAMICS OF MESOSCALE EDDIES**

Larry T. Gulliver  
Lieutenant Commander, United States Navy  
B.S., SUNY Maritime College, 2006

Submitted in partial fulfillment of the  
requirements for the degree of

**MASTER OF SCIENCE IN METEOROLOGY AND PHYSICAL  
OCEANOGRAPHY**

from the

**NAVAL POSTGRADUATE SCHOOL  
September 2017**

Approved by: Timour Radko  
Thesis Advisor

Justin M. Brown  
Second Reader

Peter Chu  
Chair, Department of Oceanography

THIS PAGE INTENTIONALLY LEFT BLANK

## ABSTRACT

Baroclinic instability in the ocean is a primary cause of mesoscale eddies, which are pockets of water in the scale of 100km that have different density, thermal, and rotational characteristics than their surroundings. First observed in the early 1900s, eddies are thought to be a predominant reason for the heat flux between the equator and the poles in both the ocean and the atmosphere. In attempt to understand this process better, this study uses a series of numerical simulations performed on high performance computing systems. The calculations are based on the Massachusetts Institute of Technology general circulation model, which is used to compare lateral heat transport between different simulations. The specific objectives of this project include

i) Comparison the direct and remote interactions of shear with topographic slope. The direct scenario is one in which the shear extends throughout the entire ocean depth and is therefore in direct contact with the sea floor, whereas in the remote scenario there is a spatial separation between the shear in the upper half of the basin and the bottom topography,

ii) Analysis of the system response to changes in the zonal and meridional seafloor slope, and

iii) Investigation of the effect of orientation changes in the mean large-scale current on cross-flow fluxes.

The lateral heat transport and diffusivity of these simulations are then compared to our analytic model, known as Growth Rate Balance, which is based on the balance between growth rate (primary) instabilities deduced from linear theory and numerically generated secondary instabilities.

THIS PAGE INTENTIONALLY LEFT BLANK



# TABLE OF CONTENTS

<b>I.</b>	<b>INTRODUCTION.....</b>	<b>1</b>
<b>A.</b>	<b>BACKGROUND .....</b>	<b>1</b>
<b>B.</b>	<b>TOPOGRAPHIC EFFECTS AND SHEAR.....</b>	<b>3</b>
<b>C.</b>	<b>GROWTH RATE BALANCE MODEL .....</b>	<b>5</b>
<b>D.</b>	<b>ORGANIZATION .....</b>	<b>6</b>
<b>II.</b>	<b>MODEL DESCRIPTION.....</b>	<b>7</b>
<b>A.</b>	<b>FORMULATION.....</b>	<b>7</b>
1.	Hydrostatic Equations.....	7
2.	Shear.....	9
3.	Zonal versus Non-Zonal Currents: Orientation .....	10
<b>B.</b>	<b>INITIAL AND BOUNDARY CONDITIONS .....</b>	<b>10</b>
1.	Size and Parameters .....	10
2.	Direct and Remote Case .....	11
3.	Zonal Case .....	13
4.	Orientation Cases.....	13
<b>C.</b>	<b>DIAGNOSTICS OF EDDY HEAT FLUX AND DIFFUSIVITY.....</b>	<b>14</b>
<b>III.</b>	<b>RESULTS .....</b>	<b>17</b>
<b>A.</b>	<b>DIRECT VERSUS REMOTE SHEAR OVER MERIDIONAL SLOPE .....</b>	<b>17</b>
<b>B.</b>	<b>ZONAL SLOPE .....</b>	<b>22</b>
<b>C.</b>	<b>ORIENTATION.....</b>	<b>22</b>
<b>IV.</b>	<b>COMPARISON WITH GRB.....</b>	<b>27</b>
<b>A.</b>	<b>THEORY .....</b>	<b>27</b>
<b>B.</b>	<b>RESULTS .....</b>	<b>29</b>
<b>V.</b>	<b>DISCUSSION AND CONCLUSIONS .....</b>	<b>31</b>
<b>VI.</b>	<b>RECOMMENDATIONS.....</b>	<b>33</b>
	<b>APPENDIX A. COMPLEMENTARY FIGURES .....</b>	<b>35</b>
	<b>APPENDIX B. DATA TABLE .....</b>	<b>37</b>

<b>LIST OF REFERENCES .....</b>	<b>39</b>
<b>INITIAL DISTRIBUTION LIST .....</b>	<b>43</b>

## LIST OF FIGURES

Figure 1.	Perpetual Ocean Image. Source: NASA Goddard Space Flight Center (2011). .....	2
Figure 2.	Diagram of the Direct (left) and Remote (right) Shear Scenarios .....	12
Figure 3.	Diagram of Zonal Shear Scenarios .....	13
Figure 4.	Diagram of Orientation Case Scenarios.....	14
Figure 5.	Direct Versus Remote Case Temperature Flux Comparison at Full North and Full South Gradients .....	17
Figure 6.	Direct Case Mean Meridional Temperature Flux and Diffusivity Versus Slope .....	18
Figure 7.	Eddy Thermal Flux in Upper Half of Remote 1100-meter Case .....	19
Figure 8.	Thermal Diffusivity in Upper Half of Remote 1100-meter Case .....	19
Figure 9.	Eddy Thermal Flux in Upper Half of Remote 3300-meter Case .....	21
Figure 10.	Thermal Diffusivity with $S_{opt}$ and $S_{int}$ , Upper Half of Remote 3300-meter Case.....	21
Figure 11.	Zonal Slope Flux Comparison .....	22
Figure 12.	Orientation Scenario CFF .....	23
Figure 13.	Orientation Scenario CF-DIFF .....	24
Figure 14.	Angle of Mean Flow (right) and Magnitude of Mean Flow (left) .....	25
Figure 15.	Schematic of GRB Model. Source: Radko et al. 2014.....	27
Figure 16.	Three Timesteps of Model Potential Vorticity .....	28
Figure 17.	3-D MITgcm 3300 m Diffusivities compared to GRB .....	29
Figure 18.	3-D Captures of 1100-meter Direct and Remote Model Runs .....	35
Figure 19.	Orientation CFF with Orientation Diagram for Visual Reference.....	36
Figure 20.	GRB with 3-D 3300-meter and Quasi-Geostrophic Comparison .....	36

THIS PAGE INTENTIONALLY LEFT BLANK

## LIST OF ACRONYMS AND ABBREVIATIONS

ACC	Antarctic Circumpolar Current
$\beta$	Coriolis Beta-effect
BI	Baroclinic Instability
CF-DIFF	Cross-Flow Diffusivity
CFF	Cross-Flow Thermal Flux
$K_T$	Thermal Diffusivity
MITgcm	Massachusetts Institute of Technology general circulation model
NS	Navier-Stokes equations
$S_{opt}$	Calculated Optimal Slope
$S_{int}$	Interpolated Optimal Slope
$Q_f$	Thermal Heat Flux
QG	Quasi-Geostrophic
U	Along-flow velocity, representative of orientation
V	Cross-flow velocity, respective of orientation

THIS PAGE INTENTIONALLY LEFT BLANK

## ACKNOWLEDGMENTS

First, I want to acknowledge my Naval Postgraduate School cohort; Jeff Scooler, “Submarine” Andy West, Dave Lorfeld, Alonzo Ingram, Chris Ayala, A-Aron Morone, and Gary Vines. Additionally, I want to recognize all my fellow METOC and USW students, including “Timour’s Angels” from the Physical Oceanography Lab. I want to thank CDR Paula Travis for her words of wisdom, encouragement and support. She gave me the room to do what I needed to do to make this possible, especially considering my circumstances during the final portion of my time at NPS.

I also want to thank Cassie Sisti for taking the time to get me started and answering my daily plethora of questions. I am grateful for Timour Radko for teaching me numerical modeling through “Bros’ menya k volkam.” I could not ask for a better mentor. Not only did he share his knowledge of physical oceanography and mathematics, but his patience with teaching allowed me to achieve and excel. Furthermore, I am thankful to Justin Brown for helping me understand Linux and coding, and for guiding me through thermal diffusivity in the Alpha Persei Cluster.

I would also like to thank SPAWAR Systems Pacific for accepting me into its fellowship program and giving me the opportunity to make much-needed processor and visualization upgrades to the Physical Oceanography Lab at NPS, which was not only a great benefit to this research, but will benefit students for years to come.

On a more personal level, there are my boys, Kyle, Logan, and Liam, who give meaning to my life every day, and my wife, Brigitte, who made sure they were taken care of while I spent long hours behind a computer screen. Last, and most important, I thank my mother, Theresa, who, is currently in the final stage of her battle against stage-IV lung cancer. She is, and has always been, an inspiration to my work, my health and my life. I am here not only because she gave birth to me, but because her passion for education and self-improvement drove the same values within me. My mother received her GED in New York state a year before I graduated high school and continued progressing forward until she earned a

bachelor's degree in psychology from Alfred State University. Her hard work ethic and compassion for people is unmatched. Ma, this is for you.



# **I. INTRODUCTION**

Modern science has both the distinction of advancing at a very fast rate due to discoveries in technology and mathematics, and the ignominy of having advanced so quickly that society has become unaware of the many natural phenomena that still remain unexplained. This thesis explores one such topic whose effect on mixing has eluded scientists from multiple disciplines and continues to be an area of debate and research. The baroclinic instability (BI), which evolves into turbulent flows that transport heat and momentum, is a predominant source of mesoscale variability in both the ocean and in the atmosphere. The nonlinear interaction of flow components leading to growing disturbances creates large-scale flows that can be easily identified in nature through in-situ and remote observations (Kamenkovich et al. 1986). These disturbances break off into energetic, relatively long-lasting circular features known as eddies.

## **A. BACKGROUND**

Eddies are everywhere! In the atmosphere, they can be seen in various forms, such as that of mid-latitude extratropical cyclones. Mesoscale eddies are features that dominate the ocean basins, especially around strong oceanic current systems like the Gulf Stream or the Antarctic Circumpolar Current (ACC), and are scientifically important for many reasons: For one, eddies are believed to be the source of more energy than any other ocean motion. Accordingly, they also transport tracers, chemicals, and nutrients, making them a cross-disciplinary topic of study (Robinson 1983). One of the greatest aspects of eddies is the transfer of heat from the tropics to the poles; thus eddy heat transport is believed to be a major contributor to the balance of the global heat budget in both the atmosphere and the ocean. Without large-scale eddy transport in the atmosphere, for example, the mean meridional circulation would be too balanced to explain the actual bulk energy transport (Green 1970). Figure 1 illustrates a satellite-derived image of eddies in the Gulf of Mexico and in the Gulf Stream.

Ocean eddies have spatial scales ranging anywhere from thousands to hundreds of thousands of meters, and time periods varying from weeks to years (Robinson 1983).

Because of this, parameterizations of eddies in climate models remain a major source of uncertainty which can lead to considerable inaccuracies in model predictions (Gent and McWilliams 1990). This feature is rather unfortunate, considering the importance of eddies to global heat budgets and in enhancing model accuracy in the long-range forecasts. For example, our inability to properly represent eddies serves as a potential cause of great uncertainty in ice melting in Arctic Ocean models (Maslowski and Lipscomb 2003). Unphysical eddy closure models can parameterize heat flux to the south for places like the Canadian Basin where northward (positive) heat flux is observed in nature (Steiner et al. 2004). The inadequate parameterization of eddies diminishes accuracy and customer confidence.

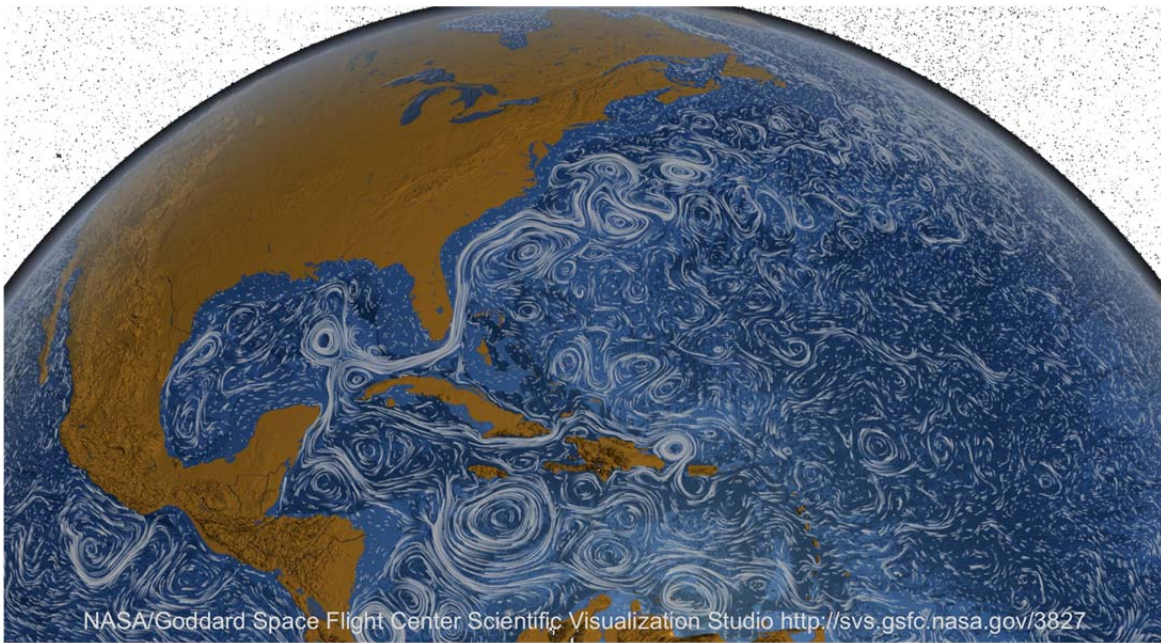


Figure 1. Perpetual Ocean Image. Source: NASA Goddard Space Flight Center (2011).

Traditionally, studies of ocean eddies have been more theoretical than observational. Pre-satellite eddy observations were few and far between. Eddies were first documented by Ben Franklin's grandnephew, Jonathan Williams, who noted a "warm core ring" while monitoring sea surface temperatures and velocities in the Gulf

Stream (Robinson 1983, Williams 1793). Observations for these “rings” was noted again in the 1930s by P.E. Church who discovered warm core eddies while examining ship thermograph records from Gulf Stream transits (Church 1932, 1937). Iselin (1936) followed this up with deep-water temperature and salinity samples taken from *The Atlantis*, from which he concluded these rings to be a permanent feature. By the 1970s, teams of scientists from around the world teamed up on surveys such as MODE<sup>1</sup> and POLYMODE, which was the largest joint U.S.–U.S.S.R. experiment of its time (Robinson 1983). Now, with the use of satellites, eddies can be observed and tracked around the globe on a daily basis. Additionally, high performance computer systems and GCMs (General Circulation Models) can realistically model the ocean in three dimensions with increasing speed and resolution. Although we may not know as much about mesoscale variability as we would like, technology has given us the advanced tools necessary that we may one day be able to solve many of Earth’s mysteries (Knauss 2000).

## **B. TOPOGRAPHIC EFFECTS AND SHEAR**

Of the many topics that require further investigation with regard to ocean eddy dynamics, the effects of topography on synoptic eddies is rapidly gaining attention of the oceanographic community. There are many ways that bottom topography can impact the physical ocean processes such as sea floor roughness, smooth versus rocky geologic features, and sea floor gradient. Observations indicate that roughness on sloped topography, even in the deep ocean abyss, will enhance vertical mixing and turbulent diffusivity (Polzin et al. 1997, Dewar 1998). This creates an issue with models that have a bathymetric resolution too coarse to represent roughness, which may cause inaccurate estimates of diffusivity and other flow properties, especially near the sea floor. This inaccuracy can be especially prevalent when attempting to model processes like internal waves or eddies (Goff and Arbic 2010). Thus, there is a need for good synthetic parameterization of this roughness, particularly with lower-resolution models.

---

<sup>1</sup> Mid-Ocean Dynamics Experiment.

Bottom relief, or slope, is known as a generating mechanism for synoptic variability. There are various ways slope can affect large- and meso-scale patterns. For example, topographic Rossby waves are a low-frequency phenomenon that can disappear when the wave is no longer in contact with the sea floor. Additionally, flow over bottom irregularities, such as sea mounts and guyots, can create instabilities which, due to the conservation of potential vorticity, can create cold core eddies above them with warm core eddies downstream (Kamenkovich et al., 1986). Topographic stress generated on these eddies can create secondary circulations which may increase upwelling and sea surface height (Holloway 1987). Sutyrin and Grimshaw (2005, 2010) considered the effects of sloping topography by applying surface-intensified circular vortices on a  $\beta$ -plane in a two-layer model with reduced gravity approximation. In their experiment they specifically looked at frictional effects on deep-ocean flows evaluating the topographic orientation effects using the  $\beta$ -drift with either along-slope or cross-slope components (Sutyrin and Grimshaw 2005). Our knowledge of the way various slopes affects eddy trajectory, for example, and how it changes the structure of the eddy as it forms, is still developing (Robinson 1983).

A third type of effect caused by bottom relief is the impact it has on the stability of the current itself. As we will discuss in the next chapter, zonal currents can be maintained in the ocean without external forces. In a stratified system with a flat (uniform depth) seafloor and zonal current, shear that remains vertically uniform can be completely stable with the only varying parameter being the Coriolis force: a fictitious force that changes with latitude as measured by the aptly-named  $\beta$ -effect, (1), (Kamenkovich et al. 1986).

$$\beta = \frac{\partial f}{\partial y} \quad (1)$$

Keeping all the same background conditions, the addition of a bottom slope can create instability (Charney and Flierl 1981). Green (1970) also noted the importance of shear in meridional heat flux and that constant shear in the troposphere would create an entropy flux that was independent of height. In this, he suggested that when there is inconsistent shear in the vertical, the heat flux can change sign. If this holds true in the

ocean, we could expect that negative values of heat transfer exist below layers of current-induced shear. The remote case in our experiment is an example of inconsistent shear. This invites the question of how the slope of the topography in a motionless lower layer will impact the heat flux in the upper remote layer, and if there will be a conservation effect that will shift the sign of heat flux at particular depths, particularly below the level of no shear.

In this study, we attempt to isolate the effect of slope on eddy dynamics by using high-resolution numerical simulations in a hydrostatically balanced, eddy-resolving model. We analyze the equilibrium dynamics of BI in an idealized environment and compare meridional diffusivity of a flat bottom case with the diffusivity over various slopes. Meridional slope should have a de-stabilizing effect on shear (Chen and Kamenkovich 2013) which should affect the eddy-transfer process. It will be shown that where slope exists, there is an increase in bottom interaction, and a decrease in stability, both of which enhance eddy formation. The question we look to answer is this: How will increased positive and negative (north and south) slopes affect large-scale eddy-induced transfer?

### **C. GROWTH RATE BALANCE MODEL**

One of the great difficulties with our understanding of eddy dynamics is the non-linearity of BI. In recent decades, many attempts have been made to explain mesoscale variability in terms of analytical models. Because mesoscale variability is non-linear, full-fledged models would be computationally prohibitive and mathematically difficult (McWilliams 2011). Several researchers, such as Thompson (2010) and Visbeck et al. (1997), have come up with different unique ways to simplify this reasoning using analytical models. One of these theoretical models, which was developed in 2014, is known as the growth rate balance model (GRB). This model is based on the assumed balance between primary ( $\lambda_1$ ) and secondary ( $\lambda_2$ ) linear modes of instability, which are linked with an empirical constant ( $C$ ). This paper will compare our 3-D model results with those of the GRB model (Radko et al. 2014).

## **D. ORGANIZATION**

The following chapters of this thesis will contain the model description as it is used in MITgcm. This includes the stability theory that explains how the model creates eddies. We will then explain the initial conditions and boundary conditions, rationale for the conditions that were chosen, and differences between the types of model runs that were conducted in this experiment. Afterward, the diagnostic tools will be discussed before moving on to Chapter III, numeric results, which will include data, charts and snapshots that best represent the data and new discoveries. Following that will be our comparison with GRB theory results in Chapter IV, discussion and conclusions in Chapter V then recommendations for future research in this topic in Chapter VI.

## II. MODEL DESCRIPTION

### A. FORMULATION

An important step in modeling ocean eddies is to understand how BI is created within the model. This chapter gives us a description of the model dynamics, explains the assumptions, and outlines rationale behind input parameters.

#### 1. Hydrostatic Equations

In this project, we will look at BI in terms of a hydrostatic, continuously stratified model with a uniform horizontal velocity decreasing with depth. Of the three options, hydrostatic, quasi-hydrostatic and non-hydrostatic, the former was chosen for the numeric representation. Although the non-hydrostatic model is the preferred choice because it is the most general, it is also the most complex and processor intensive for a numeric model. The hydrostatic model can be as effective as either of its counterparts in large-scale scenarios (Marshall et al. 1997). By scaling the dimensions of the model, a determination can be made that hydrostatic approximation is valid. Our length scales are 2000 km, thus  $L = 2 \times 10^6$  m. The height of our basin is 3.3 km, making  $H \approx 3 \times 10^3$  m, our average meridional velocity is  $0.075 \text{ m}\cdot\text{s}^{-1}$  in the remote case and  $0.15 \text{ m}\cdot\text{s}^{-1}$  in the direct which we can approximate  $U \approx 0.1 \text{ m}\cdot\text{s}^{-1}$ . Using a standard sea-water potential density of  $1 \times 10^3 \text{ kg}\cdot\text{m}^{-3}$ , which means that—with a temperature difference from surface to bottom of five degrees—we can assume a change in density over depth (based on temperature) of  $1 \text{ kg}\cdot\text{m}^{-3}$ . Therefore, we can calculate our buoyancy frequency using Equation (2) below to be  $N \approx 1.7 \times 10^{-3} \text{ s}^{-1}$ .

$$N^2 = -\frac{g}{\rho} \frac{\partial \rho}{\partial z} \quad (2)$$

Here,  $g$  is the standard gravitational constant of  $9.8 \text{ m}\cdot\text{s}^{-2}$  and  $\rho$  is water density, which will be described in Section B. In the direct case, the velocity structure of the basic state is as follows with  $v$  representing meridional velocity and  $u$  representing zonal velocity with the subscripts indicating their vertical location in the water column.

$$\begin{aligned}\bar{v} &= 0, \bar{u}_{surface} = u_{\max}, \bar{u}_{bottom} = 0, \\ \frac{\partial \bar{u}}{\partial z} &= \frac{(\bar{u}_{surface} - \bar{u}_{bottom})}{-z}.\end{aligned}\tag{3}$$

In the remote case, however, these expressions change to

$$\begin{aligned}\bar{u}_{surface} &= u_{\max}, \bar{u}_r(h = \frac{z}{2}) = 0, \\ \frac{\partial \bar{u}}{\partial z} &= \frac{\bar{u}_{surface} - \bar{u}_r}{z \frac{1}{2}}.\end{aligned}\tag{4}$$

In both cases, remote and direct, the velocity fields are related to the temperature patterns through the thermal wind balance:

$$\frac{\partial \bar{T}}{\partial y} = -\frac{f}{g\alpha} \frac{\partial \bar{u}}{\partial z}.\tag{5}$$

Initial boundary conditions were adopted based on Radko et al. (2014) with changes made to reflect a deeper open-ocean seafloor that would better represent conditions in the mid-ocean basins. This is particularly pertinent to the Southern Ocean, which reaches depths over 5 km. Because the model setup had already been tested, this became the basis for this experiment. This experiment includes  $\beta$  of  $1 \times 10^{-11}$  and standard Coriolis parameter of  $1 \times 10^{-4} \text{ m}^{-1} \cdot \text{s}^{-1}$ . Density stratification in our model ocean basin was created by assuming uniform salinity of 35 psu, thereby making density solely a function of temperature. Velocity is induced via Equations (3) and (4). In order to create both a horizontal and vertical stratification, the equation for thermal wind (5) is used in conjunction with shear gradient to generate a temperature gradient in the model (Kamenkovich et al. 2009). This temperature gradient corresponds to an approximate  $10^\circ\text{C}$  overall variation in the vertical and  $14^\circ\text{C}$  in the horizontal. A randomly generated temperature variation of magnitude  $0.10^\circ\text{C}$  was induced throughout the model, which disrupts the initial stratification enough to facilitate instability once it is acted on by shear.



## 2. Shear

One of the main drivers of BI is the shear. Vertical shear provides a key component into destabilizing the stratification and thereby inducing instability. For this study we chose a magnitude of shear that is observationally reasonable capable of generating BI. By testing standard surface current velocities,  $u_{surface}$ , with a gradient of decreasing velocity with depth,  $-\frac{\partial u}{\partial z}$ , a standard gradient was determined that is used in all our shear and depth scenarios. In this research, two shear configurations and two depths are compared. The first configuration is the direct case where the shear was induced throughout the water column, reducing linearly in intensity with depth until  $u_{bottom} = 0$ . The second configuration is the remote case, which is where the shear was applied to the upper half of the basin, but the lower half was given motionless initial conditions. No meridional flow is initially induced and therefore any flow in the  $y$ -direction is caused by dynamic effects. In doing this, a comparison can be made between both the direct and remote shear scenarios and between the different meridional slopes. By measuring the eddy heat flux, we can determine if there is a remote effect on the topography on the background current, and the role that bottom slope plays on ocean heat transport.

The remote case scenario was conducted at two different depths: 1100 m and 3300 m. In order to compare the shear effects between scenarios at different depths, we required that the shear gradient remain the same instead of the mean or maximum velocities of zonal flow. Therefore, for the 3300m case, the surface velocity measured  $0.15 \text{ m}\cdot\text{s}^{-1}$  and reached zero velocity at a depth ( $z$ ) of 1550 m whereas the 1100 m case measured  $0.05 \text{ m}\cdot\text{s}^{-1}$  reaches zero velocity at 550 m. This gives give us a shear gradient that is equivalent for both depths, despite a greater area covered by shear in the 3300-m case. Thus, our comparisons are based strictly on a comparable shear gradient rather than separate shear gradients with the same surface velocity as illustrated by

$$\frac{\partial u}{\partial z}(h_0 = 1100m) = 0.9091e^{-5} s^{-1} = \frac{\partial u}{\partial z}(h_0 = 3300m). \quad (6)$$

### 3. Zonal versus Non-Zonal Currents: Orientation

Because of the Coriolis force, a current in the zonal direction is the only flow that can be maintained without the effects of outside forces (Kamenkovich et al. 1986). In this experiment, the flow direction is turned at  $30^\circ$  intervals over a flat bottom basin, and the impact of the rotation on the cross-current thermal flux (CFF) is analyzed. The magnitude of horizontal velocity is  $\bar{U} = \sqrt{U^2 + V^2}$ , where  $U$  represents along-flow current and  $V$  represents the across-flow current. The term “flow” in this context describes the initial background current in the direction of orientation. Lower case  $x$  and  $y$  represent the longitudinal and latitudinal axes, which is standard in our zonal flow simulations, but in the orientation cases we use  $X$  and  $Y$  to indicate the along-flow and cross-flow axes respectively. Because the dimensions of the basin remain the same, and the basin-relative flow remains the same, the value of any diagnostic in  $Y$ , although no longer meridional, is our desired quantity. The thermal gradient also changes with each rotation, and therefore, it is the  $\beta$ -effect that will provide the physical difference between orientation runs.

It should be emphasized that, in the orientation cases the time mean flow is not strictly oriented in the  $X$ -direction. Therefore, the mean temperature flux in  $Y$  includes a cross-flow component associated with the advection of heat by time-mean velocity, which must be accounted for in order to determine CFF. This is done in the post-processing analysis as follows:

$$\overline{T'V'} = \overline{TV} - \bar{T}\bar{V}. \quad (7)$$

## B. INITIAL AND BOUNDARY CONDITIONS

### 1. Size and Parameters

In determining the size of the basin, a few principles of eddy dynamics were implemented. Since mesoscale eddies are in the scale of tens to hundreds of kilometers wide, the horizontal dimensions of the box had to be large enough to resolve 100 km features while the resolution also had to be fine enough to encompass the smaller eddies. In particular, baroclinic radius of deformation ( $R_d$ ) must be resolved in order to ensure that baroclinic instability is properly represented. Inherently, the Brunt-Väisälä buoyancy

frequency ( $N$ ) determines radius of deformation. To simplify the equation for determining density stratification, salinity was kept constant at 35 psu, which means that density( $\rho$ ) becomes a function of temperature:  $\rho = \rho(T)$ . Because of this, there is a direct relationship between our temperature gradient and pressure gradient, which can be used to estimate buoyancy. The expressions below use the equation of state to replace density with temperature and solve for  $R_d$ . Note that  $\alpha$  is the thermal expansion coefficient.

$$R_d = \frac{Nh}{f} \quad (8)$$

$$\partial S = 0, \frac{\bar{\rho} - \rho_0}{\rho_0} = \alpha(\bar{T} - T_0) \rightarrow \frac{\partial \rho}{\partial z} \approx \frac{\partial T}{\partial z} \quad (9)$$

$$N = \sqrt{-g \frac{\partial \rho}{\partial z}} \approx \sqrt{-g \alpha \frac{\partial T}{\partial z}} \quad (10)$$

This equation gives a calculated  $R_d$  of approximately  $2.4 \times 10^4$  m, or 24 km for the 1100-meter runs and  $4.20 \times 10^4$  m (42 km) for the 3300-meter case. This is consistent with the size of mesoscale eddies. This estimate led to the optimal choice for basin size for this experiment of 2000 km by 2000 km, as the basin had to be wide enough to contain a large number of eddies. Additionally, the horizontal resolution is also a factor since too coarse a resolution will not be able to simulate eddies, and too fine a resolution will cause model run times to increase dramatically. Two-kilometer resolution was chosen as it is  $1/10^{\text{th}}$  the scale of concern of  $R_d$  for the 1100-meter case.

## 2. Direct and Remote Case

As mentioned in the introduction, two major flow regimes were introduced into the original research plan, which have been aptly named the direct and remote cases. The direct case is perhaps the more straightforward of the two as the shear is exerted throughout the water column by introducing a surface current that decreases in magnitude linearly with depth all the way to the seafloor. Thus, the shear is present throughout the water column and is only inhibited at the sea floor. In the remote case, the shear is

present only in the upper half of the water column, and the velocity becomes zero at half depth. Thus, the lower half of the water column is completely motionless initially. Figure 2 is a visualization of the remote and direct shear scenarios. A 3-D visualization can be seen in Appendix A (Figure 18).

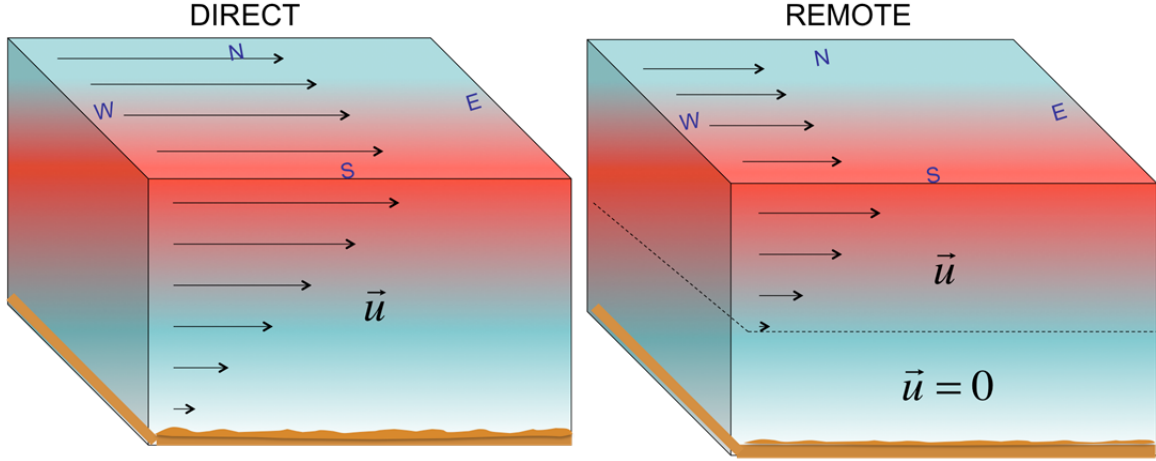


Figure 2. Diagram of the Direct (left) and Remote (right) Shear Scenarios

This motionless region is not a “lower layer” and should not be confused with a two-layer model because the stratification in the upper and lower half is continuous. The lower half is merely a region of no initial zonal current, and therefore, any flow that occurs in the lower layer is due to baroclinic instability effects induced in the upper layer. Also, the magnitude of the shear is the same across the direct and remote cases is the same. That is the linear decrease in velocity is the same. This also means that the velocity on the surface is twice the value in the direct case. This allows us to maintain the same shear magnitude despite having larger surface speeds with the direct flow:

$$\begin{aligned} \overline{\frac{\partial u_{dir}}{\partial z}}(h_0 = 1100m) &\approx 0.055ms^{-1}, \overline{\frac{\partial u_{dir}}{\partial z_{1/2}}}(h_0 = 1100m) \approx 0.026ms^{-1} \\ \overline{\frac{\partial u_{dir}}{\partial z}}(h_0 = 3300m) &\approx 0.15ms^{-1}, \overline{\frac{\partial u_{dir}}{\partial z_{1/2}}}(h_0 = 3300m) \approx 0.078ms^{-1}. \end{aligned} \quad (11)$$

### 3. Zonal Case

The previous model compared several cases of various meridional, or north—south slopes. In an effort to mimic the somewhat of a mid-Atlantic ridge, a series of runs were performed to determine the effects of topographic slope in a zonal, or east—west, direction, as depicted by Figure 3. In these scenarios, the depth of the water remained constant in  $y$ , but changed over  $x$  with an apex at length  $x/2$ ; thus, the flow is perpendicular to the bottom gradient. This also means that potential vorticity of the mean flow in the direct case will obviously be affected by the height of the water column as seen by Equation (12). However, the impact of the bottom topography in the remote case will be less certain. Additionally, because the zonal slope can deflect the initially zonal flow, the background meridional flow will have to be taken into account when evaluating the eddy-induced transport. Equations for the potential vorticity and zonal slope are

$$\frac{f + \zeta}{h} = \text{const} \quad (12)$$

$$\frac{\partial h}{\partial y} = 0, \frac{\partial h}{\partial x_{(0 \rightarrow x/2)}} = S_m, \frac{\partial h}{\partial x_{(x/2 \rightarrow x)}} = -S_m. \quad (13)$$

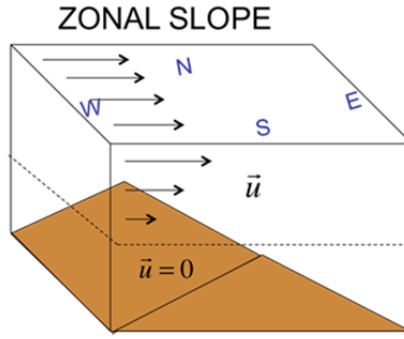


Figure 3. Diagram of Zonal Shear Scenarios

### 4. Orientation Cases

For the purposes of simulating initial flows for various orientations, we chose to retain the flow direction relative to the computational domain and re-orient the basin in order to simplify our analysis and allow us to induce periodic boundary conditions along the flow. To simplify our post-processing, we retain the flow direction and shape and re-

orient the basin. Future experiments may wish to try alternative methods of measuring and calculating orientation output across the flow for comparison. Rotating the basin involved converting from Cartesian grid, which we used on our other runs, to a spherical grid. The orientation was controlled by using Eulerian coordinates to turn the basin around the z-axis using the scale 1degree latitude = 111 km. This gave us a  $dx$  and  $dy$  of  $\sim 1.8^\circ$  vice 2 km. Figure 4 depicts the orientation scenarios and their respective angles.

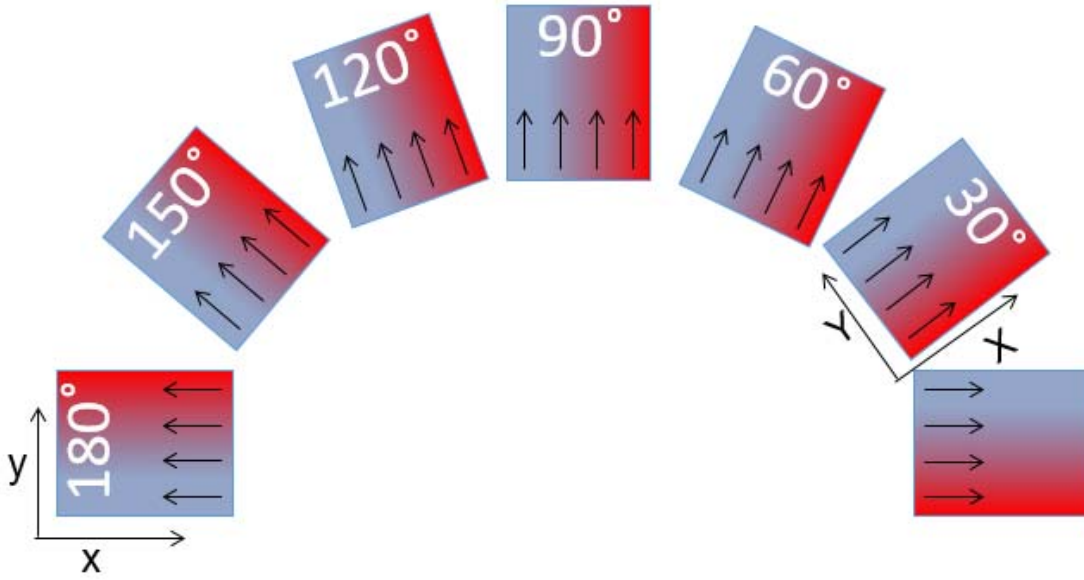


Figure 4. Diagram of Orientation Case Scenarios

### C. DIAGNOSTICS OF EDDY HEAT FLUX AND DIFFUSIVITY

In order to evaluate the impact of topographic effects on mesoscale variability, we must anticipate what variables that our numeric model outputs that we would expect to see change. This section outlines some of the rationale behind our diagnostic tools based on the relationships to each other and to how we would expect them to be impacted under different conditions. Because of our model setup with a current that is strictly zonal (except for the “orientation” runs), meridional motion is mostly caused by the baroclinic instability. Therefore, our measurement of any transient displacement in  $y$ -direction will reflect the intensity of mesoscale variability. This is important because in order to

determine the effects of mesoscale variability, it should be clearly isolated from any direct effects of background flows. To accomplish this, we simplify the eddy equations of motion and make our initial background currents purely zonal flow. Inherent in this simplification is the lack of any rotational or non-meridional transport and so divergent and rotational components are not isolated (Radko et al. 2014). Note that for the orientation case, this simplification is only possible by applying values of  $x$  and  $y$  as “along-flow” and “across-flow,” respectively. Additionally, non-eddy effects are removed by removing mean flow from our  $v$ -velocity.

As previously mentioned, mesoscale eddies are an important component in the transfer of heat from the equatorial region to the poles. This means eddies are also large contributors in maintaining the heat balance for our planet. Because the stratification in our idealized basin is maintained through temperature and not salinity, we are able to truncate our equation of state to essentially replace density gradient with thermal gradient. This allows us to approximate density with temperature, and therefore temperature becomes a key diagnostic variable. MITgcm allows you to output both temperature and heat flux in both  $x$  and  $y$  directions (Menemenlis and Fukumori, 2005). Because we are taking our values over time and we can average gridpoint values over the entire model area and over all the equilibrium time periods in order to get one value for the average temperature flux ( $Q_f$ ) over the period from when the model reaches baroclinic equilibrium to the last integration output.

$$Q_f = \overline{V'T'} \quad (14)$$

If the heat flux is required, it can be trivially computed from the temperature flux as follows:

$$Q_{hf} = \rho C_p Q_f, \quad (15)$$

where  $C_p \approx 4000 J kg^{-1} K^{-1}$  is the specific heat and  $\rho \approx 1000 kg m^{-3}$  is the density of seawater. Thermal diffusivity ( $K_T$ ) can be obtained by dividing the temperature flux by the thermal gradient, as indicated in Equation (16).

$$T_y = \frac{\partial T}{\partial y} = \frac{T_{jj+1} - T_{jj-1}}{2\partial y}$$

$$K_T = -\frac{Q_f}{T_y}$$
(16)

Finding the overall thermal gradient in Equation (17) from the model is accomplished by averaging the temperature gradients for each gridpoint in space and time. The advantage behind diffusivity is that it can easily be compared with alternative estimates in literature and analytical models, like GRB. To maintain a statistically steady state, a relaxation condition is enforced on the surface and bottom in order to prevent unrealistic build-up of warm and cold temperatures. Additionally, all diagnostic variables are calculated only after removing the boundaries as far out as 60 km. This was necessary to be able to focus on what was occurring within the deep water basin and to avoid contamination from boundary layer dynamics. Think of this as removing the wax layer from around the cheese in order to prevent a nasty taste in your mouth.



### III. RESULTS

#### A. DIRECT VERSUS REMOTE SHEAR OVER MERIDIONAL SLOPE

We compared the initial meridional slope runs conducted in the 1100-meter basin to determine any topographic effects on eddy heat flux. We also investigated the remote scenario, where the flow and shear were not in direct contact with the seafloor, for the effects of varying the slope. There is a remote effect on eddy heat flux even without direct interaction. However, the mean total heat flux is over three times greater in the direct case than in the remote case for an equivalent slope ( $s = 2.62 \times 10^{-4}$ ) after the model reaches an equilibrium. In both cases, a south slope of the same absolute value as the north slope yields a greater meridional heat flux as seen in Figure 5.

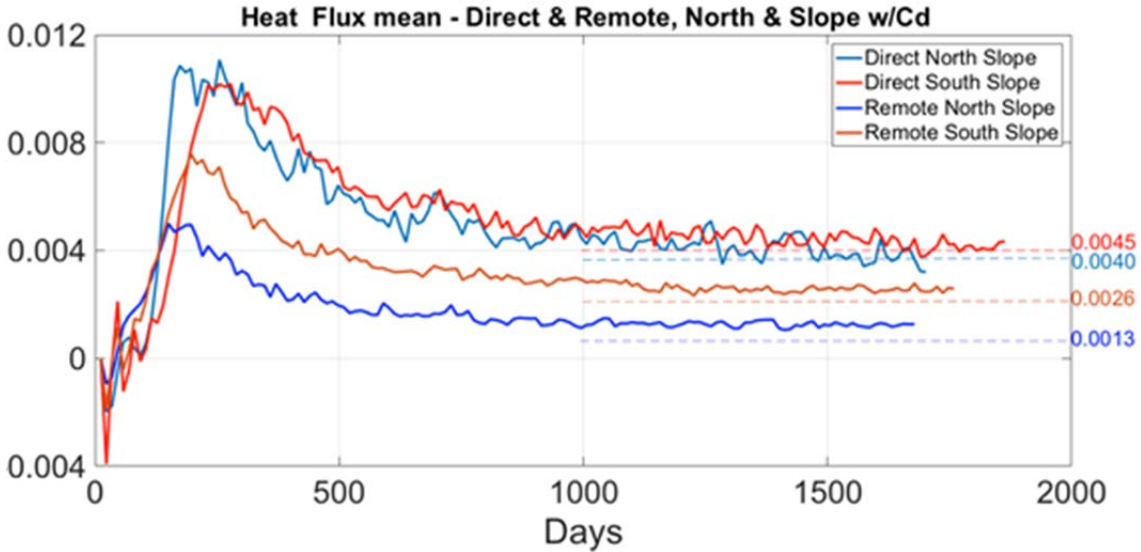


Figure 5. Direct Versus Remote Case Temperature Flux Comparison at Full North and Full South Gradients

In our direct case, variations in the meridional bottom slope are expected to affect variation in total mean heat transport. Chen and Kamenkovich (2013) observed in a two-layer model that meridional slope changes the PV gradient causing a stabilizing effect. The results of the 1100-meter model indicate that in the direct shear case, the largest mean meridional heat flux and diffusivity occur for a flat seafloor (zero slope), which

would indicate that a bottom gradient of any kind reduces horizontal diffusivity (Figure 6). However, calculating the meridional heat flux in the upper half of the basin, the remote case (Figure 7) yields the greatest flux for a slightly negative bottom slope. The same can be said for diffusivity (Figure 8) which shares the same curvature.

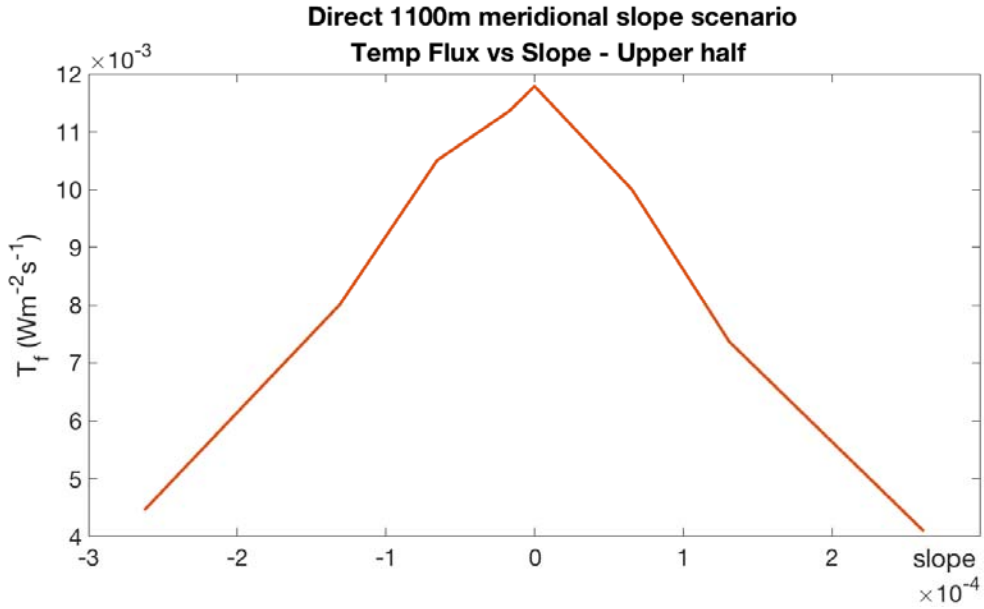


Figure 6. Direct Case Mean Meridional Temperature Flux and Diffusivity Versus Slope

One of the explanations for the weaker total heat flux in the remote case could be that the remote case is more strongly affected by conservation of potential vorticity. Perhaps this is due to the effect of the bottom drag, which may have a stronger impact on direct flows because of the solid boundary directly below the shear region; the latter feature is absent in the remote case. In order to explain the pronounced asymmetry of temperature flux in the remote case (Figure 7), we now attempt to develop a simple analytical theory predicting the slope that results in maximal heat transport. This slope, which will be referred to as the optimal slope hereafter, is computed based on the analysis of the equation for conservation of potential vorticity ( $Q_{pv}$ ), given by

$$Q_{pv} = \frac{\zeta + f}{h} = \frac{\zeta + f_0 + \beta y}{h_0 - sy} = \text{const} . \quad (17)$$

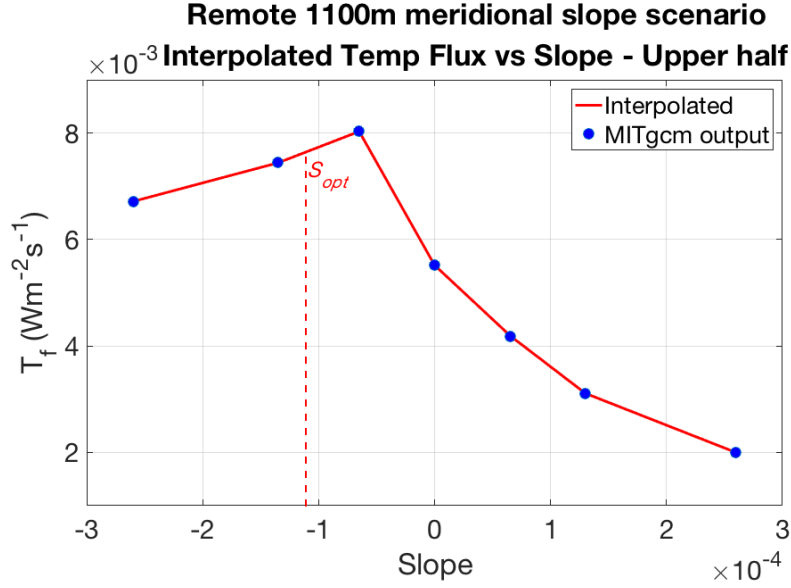


Figure 7. Eddy Thermal Flux in Upper Half of Remote 1100-meter Case<sup>2</sup>

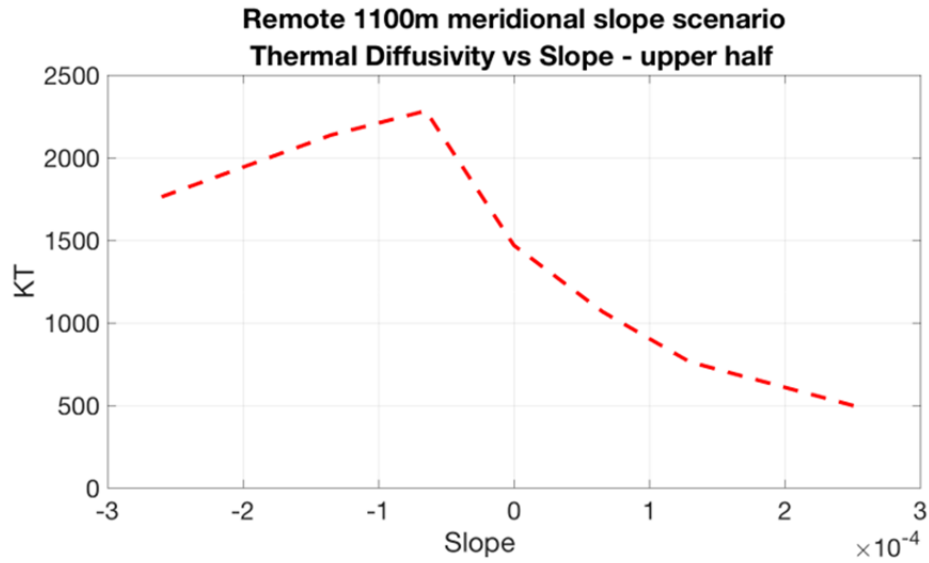


Figure 8. Thermal Diffusivity in Upper Half of Remote 1100-meter Case

Conservation of  $Q_{pv}$  implies that the meridional displacement of water columns is adversely affected by both the  $\beta$ -effect and by the slope individually. However, when both effects operate concurrently, they can counteract each other and thus have minimal

<sup>2</sup> MITgcm thermal flux output was plotted along with the calculated thermal flux for validation.

impact on the meridional displacements of water columns. By assuming that this cancellation occurs when

$$f_0 + \beta y \propto h_0 - sy \quad (18)$$

we can roughly identify an optimal slope ( $S_{opt}$ ) based on  $\beta$ ,  $f_0$  and the slope  $s$ , where  $\beta = 1 \times 10^{-11} \text{ m}^{-1} \cdot \text{s}^{-1}$ ,  $f_0 = 1 \times 10^{-4} \text{ s}^{-1}$ , and  $h_0$  is the maximum depth of the water column. This assumption can be rationalized as follows. The conservation of  $Q_{pv}$  states that if the height of the water column changes, rotational vorticity ( $\zeta$ ) resists change, and therefore,  $Q_{pv}$  is conserved through a north or south shift, which compensates for changes in  $f$ . On the other hand, if  $f$  changes, the water column will want to compensate by stretching or shrinking. Equation (18) then immediately implies

$$S_{opt} = -\frac{\beta h_0}{f_0} \quad (19)$$

This formula for optimal slope, Equation (19) shows a calculated  $S_{opt}$  of approximately  $-1.1 \times 10^{-4}$  for  $h_0 = 1100 \text{ m}$ , which is comparable to our model results. Using a splines interpolation, the value of the maximum slope based on the compared model runs is  $-0.858 \times 10^{-4}$ .

Using this same equation, the 3300-meter remote case can also be analyzed. Because the theoretical  $S_{opt}$  is a function of the base depth, it is easily estimated at three times the 1100-meter case, ( $S_{opt}(h_0 = 3300 \text{ m}) = 3.3 \times 10^{-4}$ ). However, our results are a bit more complicated than our simple theory. This meant that additional southern, or negative slope values had to be run for this case in order to find the slope great enough for our optimal case. However, even with these extreme slope simulations, the optimal slope for heat flux has not yet been attained. Figure 9 illustrates that the general shape of the slope to  $Q_f$  difference is maintained, the  $S_{opt}$  does not appear to be within the range of slopes modeled. In fact, it appears that the increased heat flux levels off below  $-4 \times 10^{-4}$  rather than tapering off sharply like they did in the 1100-meter case.

It initially appears that the optimal slope theory tends to output too gentle a slope for the  $h = 3300 \text{ m}$  case. However, taking a look at the interpolated diffusivity plot in Figure 10, the diffusivity does begin to drop off at a  $S_{int}$  of  $-4.54 \times 10^{-4}$ , which is close to

our calculated  $S_{opt}$ . A clear difference between the diffusivities and heat flux can be seen at larger slopes, whereas in the slopes calculated in the 1100-meter case, the  $K_T$  and  $Q_f$  curves were nearly identical.

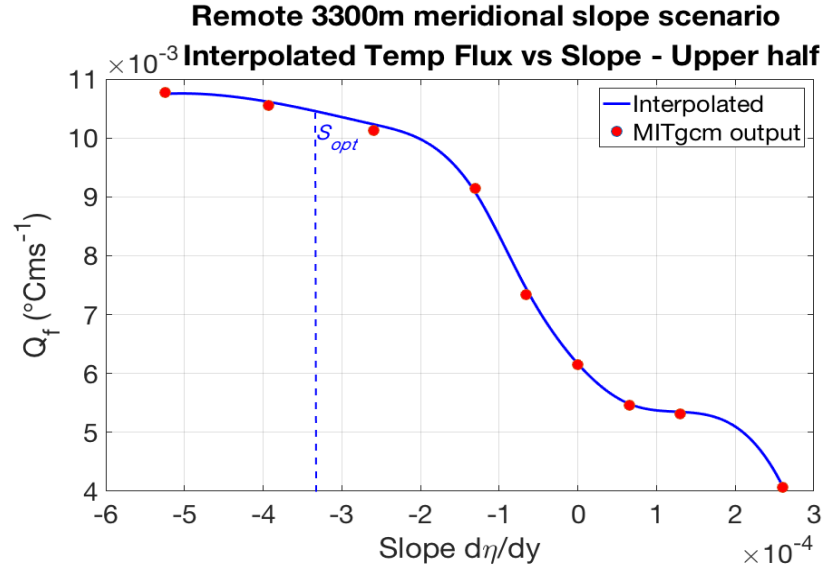


Figure 9. Eddy Thermal Flux in Upper Half of Remote 3300-meter Case

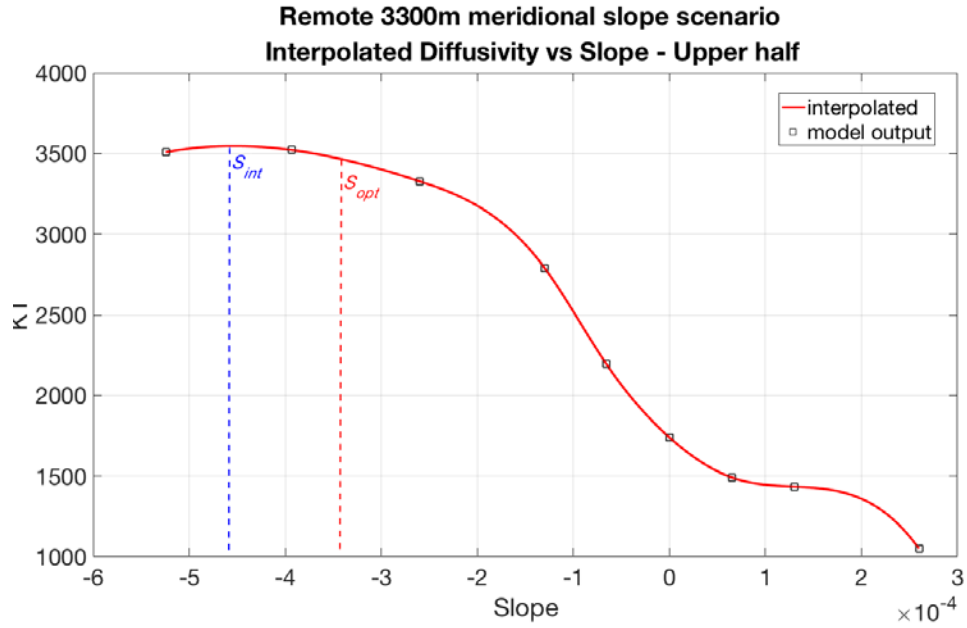


Figure 10. Thermal Diffusivity with  $S_{opt}$  and  $S_{int}$ , Upper Half of Remote 3300-meter Case

## B. ZONAL SLOPE

The zonal slope case was analyzed in the same way as the meridional slope case in order to compare the direct and remote scenarios using the two separate slopes. Results show that in both the direct and remote cases, and in both slopes, the net heat flux was equivalent to that of a flat bottom case. Singling out the  $Q_f$  observed on either the east or west side of the apex, we discover that they are noticeably large and erratic, which may be corrected if the turbulent fluxes were subtracted from the total flux. However, it is apparent to see that the southward mean flow of the western, or “uphill,” side of the basin is fully countered by the northward flow on the eastern “downhill” side. In Figure 11, the black and gold lines represent both the flat bottom case equivalent and the net  $Q_f$  for the full water column for which the values are nearly identical. This was true both for the direct and remote cases at both slope angles where the calculated difference between the net zonal and flat bottom fluxes was negligible.

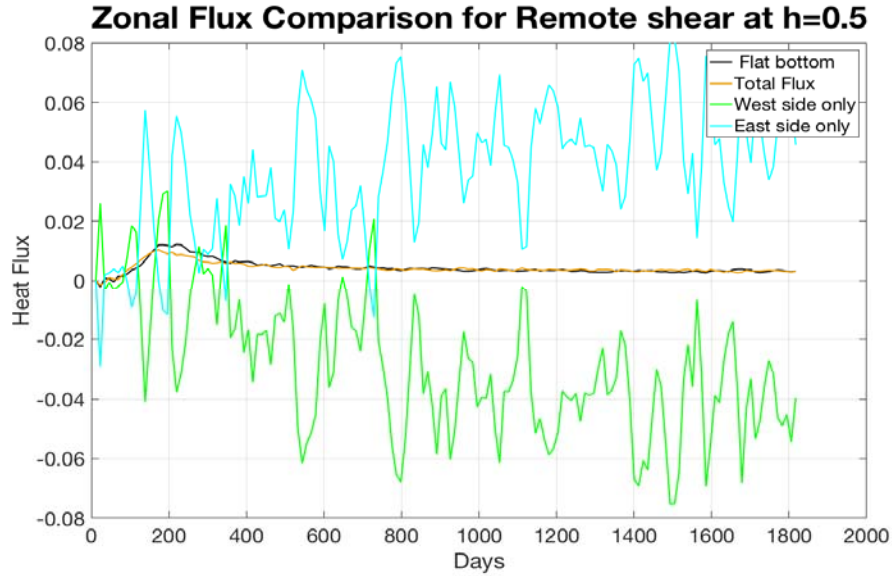


Figure 11. Zonal Slope Flux Comparison

## C. ORIENTATION

As a reminder, diagnostics for the orientation runs were calculated in the frame of reference associated with the initially imposed basic flow. In particular, we look at the

cross flow heat flux, diffusivity, and the velocity and magnitude of the mean current. Figures 12 and 13 illustrate the different CFF and CF-DIFF patterns for each value of  $\theta$ . As  $\theta$  increases, the CFF is dampened until  $\theta=90^\circ$  at which point it rises again. At  $\theta=180^\circ$  it reaches a maximum CFF, three times that of the zonal flow at  $\theta=0^\circ$  and in the polar opposite direction: southward flux instead of northward. Similar to larger slopes in the 3300-meter zonal flow model, the orientation models' CF-DIFF and CFF plots do not have the same shape. CF-DIFF, for example, reaches its minimum at  $\theta=0^\circ$  and its maximum at  $\theta=120^\circ$ . This is  $60^\circ$  out of phase with the CFF curves of both values. The results suggest that diffusivity is offset from fluxes when oriented flow is involved. Additionally, the diffusivities are approximately twice the typical values observed in the ocean. Appendix A (Figure 19) depicts Figure 12 with orientation angles for better reference.

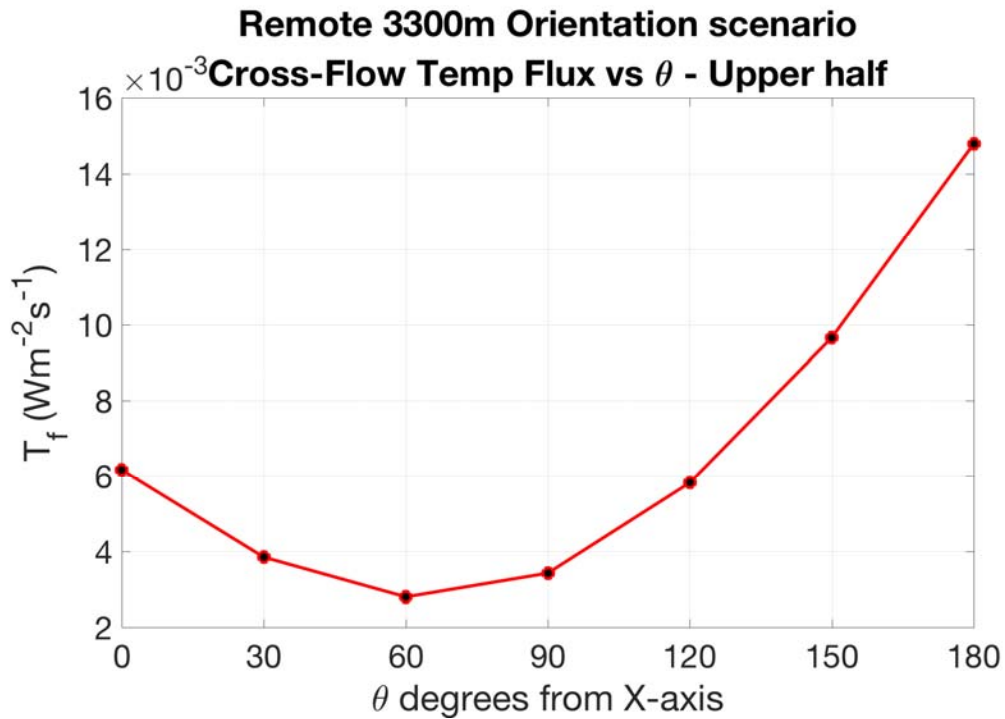


Figure 12. Orientation Scenario CFF

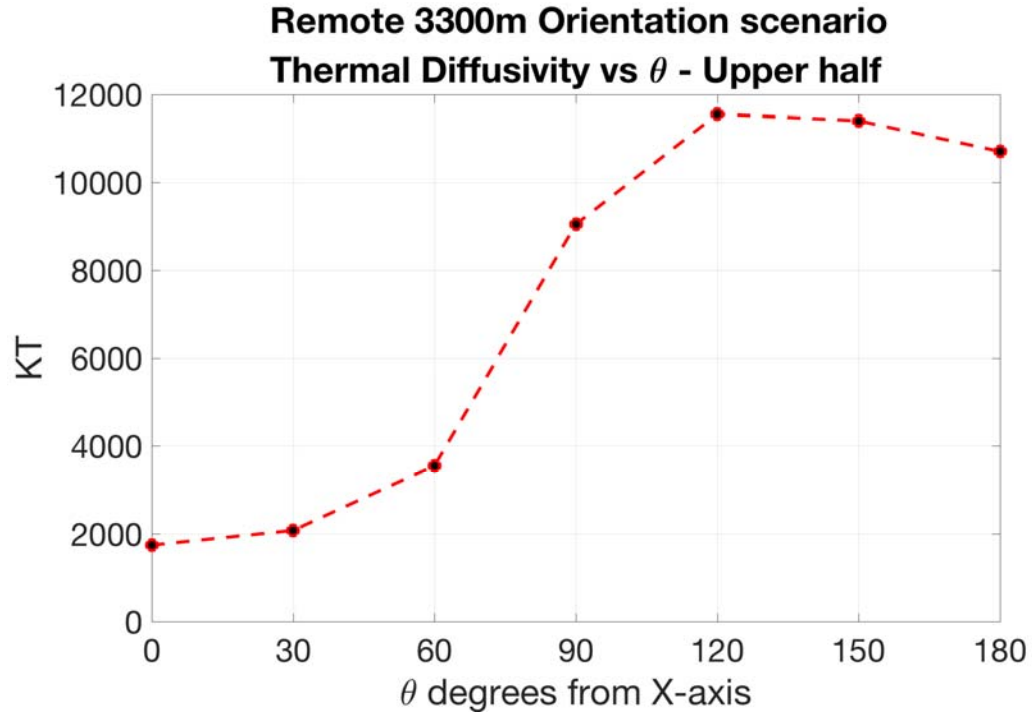


Figure 13. Orientation Scenario CF-DIFF

Mean velocities were also computed in order to identify potential changes in the properties of background flow. In Figure 14 (right), the angle of the mean flow is plotted in relative to the equator, or  $x$ -axis (magenta) and relative to the orientation of the initial flow (cyan). Not surprisingly, there is a clockwise veer for each of the non-zonal flows, which are all comparatively similar, roughly in the range of 4–12 degrees. Both of the zonal flows ( $0^\circ$  and  $180^\circ$ ) maintain their mean flow angle with the direction of background flow. However, the magnitude differences between the mean flows at different values of  $\theta$  is noteworthy. Note in Figure 14 (left) that the mean flow velocity for  $\theta=0^\circ$  is the initial value of the mean current and is therefore approximated. Initially, the sharp decrease in mean flow velocity begins like the CFF, dropping significantly and rising again all the way up to  $\theta=150^\circ$ , it then suddenly drops again around  $\theta=180^\circ$ , unlike the CFF.



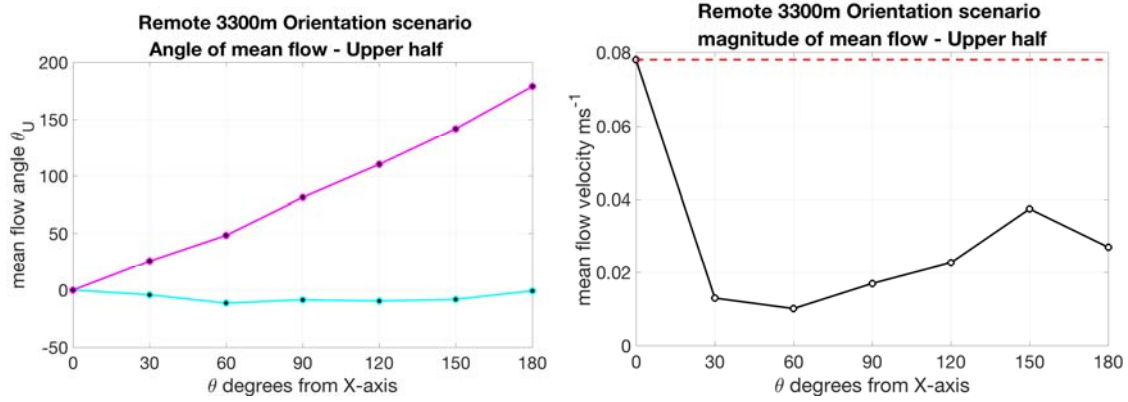


Figure 14. Angle of Mean Flow (right) and Magnitude of Mean Flow (left)

THIS PAGE INTENTIONALLY LEFT BLANK

## IV. COMPARISON WITH GRB

This chapter focuses on comparing our 3-D model data to GRB. First by briefly explaining the theory of GRB, then by comparing our 3-D MITgcm results to the GRB results for our 3300-meter remote case.

### A. THEORY

Oceanographers have often attempted to explain the non-linear effects of BI using analytical models. GRB attempts to explain BI by linking the growth rates of the primary ( $\lambda_1$ ) and of the secondary ( $\lambda_2$ ) modes of instability. Such analysis can be insightful because, as the primary mode increases in intensity, the secondary mode, which is a function of the primary, intensifies and eventually dampens the primary mode. In this theory, the two modes “compete” and, in doing so, an equilibrium state is created where the instabilities finally match each other. This “balance” can be calibrated using an empirical constant, ( $C$ ).

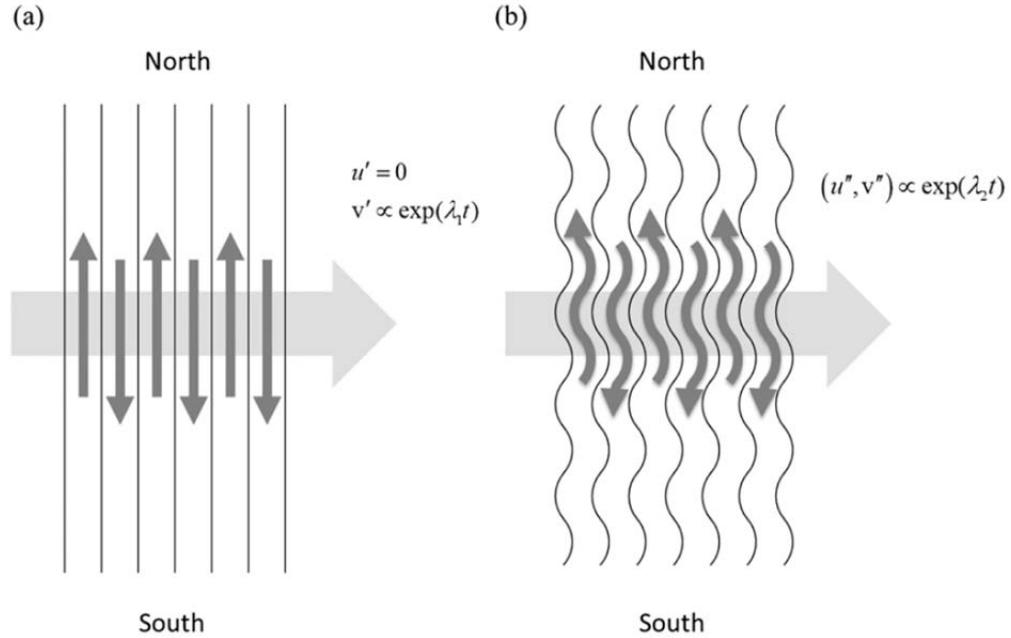


Figure 15. Schematic of GRB Model. Source: Radko et al. 2014.

One of the features of this theoretical model is that the primary modes are a function of vertical shear, bottom drag, stratification, and  $\beta$ -effect, whereas the secondary mode is a function of all of those plus the primary mode amplitude. The GRB equation can be summed up by the following:

$$\lambda_2 = C\lambda_1 \quad (20)$$

In theory, the primary mode would grow continuously if not for the secondary mode hindering its development. Likewise, if the secondary instabilities ( $\lambda_2$ ) were to dominate, the primary instabilities would be overly-dampened which would ultimately result in no eddy formation. This means the two modes must reach a balance at some point, at which the output diagnostics can be time averaged to see the mean results. Examples of this instability and its progression can be seen in a horizontal section of the numeric models as shown in Figure 16. The Growth Rate Balance theory is discussed in greater detail by Radko et al. (2014). For this paper, numerical results from 3-D MITgcm model runs will be used to compare to a 2-D Growth Rate Balance analysis. Figure 16 includes three time steps of potential vorticity from a numeric model that illustrates the progression of initial growth rate (left), the development of secondary instabilities generating wave-like patterns (center), and the resulting transient irregularities (right).

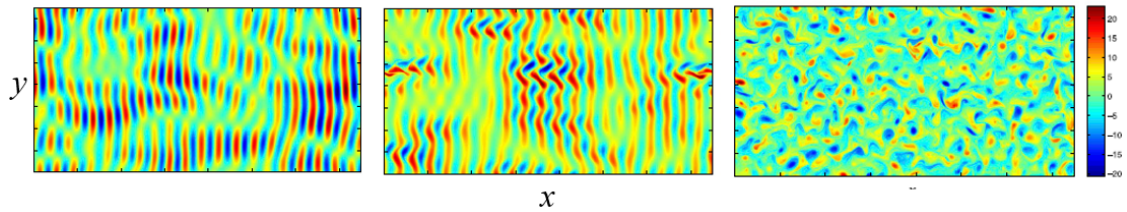


Figure 16. Three Timesteps of Model Potential Vorticity. Adapted from Radko et al. 2014.

## B. RESULTS

In determining the best fit for the GRB model, Radko et al. (2014) investigated several values of the non-dimensional empirical constant,  $C$ , that would best fit the Phillips (1951) and Eady (1949) models of linear instability. A range of 3.5-4 was determined to be the best fit, which was calibrated using PV flux. The 3-D models to which they compared to had spatial scales similar to our model, lacked sloping topography and the shear was in the direct contact with the seafloor. For this thesis, the 3300-meter remote case was plotted against calibrated values of PV diffusivity determined from GRB models for each slope at values of  $C$  from 2 to 5. Interestingly, the GRB models predict a slightly northern optimal slope. Only the diffusivities calculated from our flat bottom (zero slope) 3-D MITgcm model compared well to the GRB model, which was just under the  $C=3.5$  plot. As seen by the 3D versus  $C$  values in Figure 17, within a range of slopes from  $+2.6 \times 10^{-4}$  to  $-1.4 \times 10^{-4}$  the various diffusivities did stay within the boundaries of  $2 \leq C \leq 5$ , but for any slope outside of that range, the analytic model was not ideal.

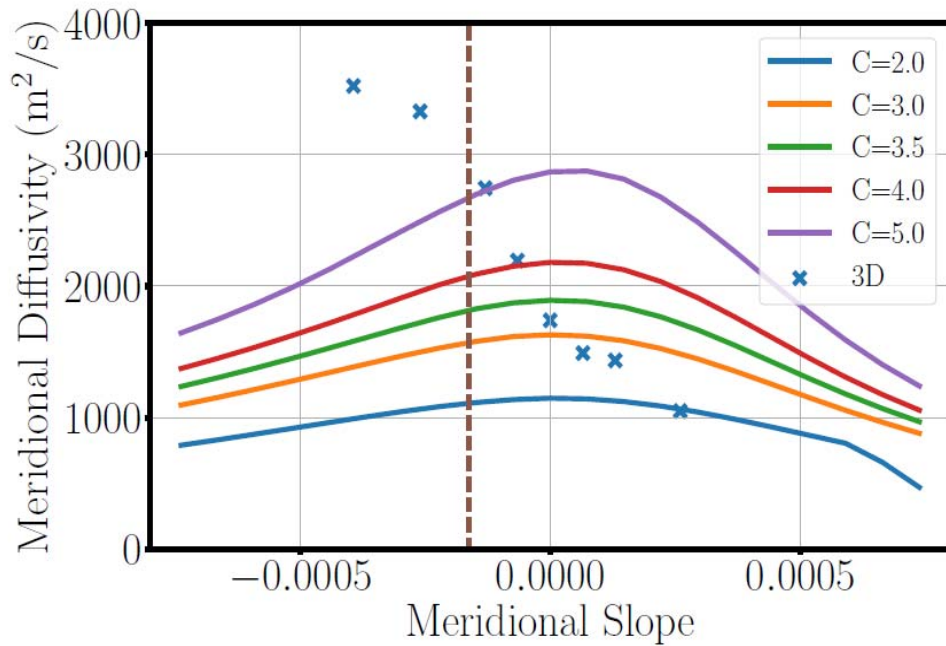


Figure 17. 3-D MITgcm 3300 m Diffusivities compared to GRB

Ultimately, the gradual bell curve of the GRB runs does not match the curve of the 3-D MITgcm plots (Figure 17). If we look at a value of  $C = 3.5$ , which is consistent for our flat bottom case, the predicted diffusivities from the GRB theory are too low for negative slopes, and it appears to be too symmetric along the y-axis. It appears that, although the GRB model compared well to the Eady model in Radko et al. (2014), where  $C = 3$  fit for each run, for our model, changing the slope of the sea floor creates variability that the GRB model does not predict. Comparisons with the quasi-geostrophic model can be seen in Appendix A (Figure 20).

Several factors may be able to explain why GRB does not do well with topographic slope. One may be the simulation depth. The 3-D model in Radko et al. (2014) was 1100-meters deep. Here, we are comparing the 3300-meter model. Second, the assumptions in the GRB model may not accurately account for topography in the basic equations. Although the GRB model accounts for topographic variation, it may not be able to represent more complex geophysical domains. Third, there may be a factor in developing BI that GRB is not able to account for. Ultimately, however, this is a good indication of why we need a better understanding of the effect bottom topography has on dynamics.

## V. DISCUSSION AND CONCLUSIONS

The first significant conclusion of this research is that the remote case shear scenario acts differently than the direct case with regard to the effect on BI. First, the intensity of heat transport in the direct case is greater given the same shear and slope. This is to be expected since the shear force covers twice the amount of volume as in the remote case. What is unexpected is that the meridional slope acts on the direct shear case differently than on the remote case. Any meridional slope dampens the heat flux in the direct case, whereas in the remote case there is a non-zero optimal slope for maximum  $Q_f$ . It should be noted that this is a large-scale experiment, but similar effects may also occur in smaller scale scenarios. This could be important in straits where there is a meridional slope with seasonally changing shear depths: a scenario where the difference in heat transfer may prove more complicated than typical parameterizations account for (Spall and Chapman 1998).

The distinct optimal slope of the remote case is perplexing since, based on  $\beta$ -effect alone, the direct case should also have a non-zero optimal slope. One possibility is that in the direct case, shear acting directly on the motionless seafloor is more influenced by bottom drag. Since the shear is directly impacted by the bottom drag, the frictional forces due to any increased slope overcome the variation caused by the  $\beta$ -effect, therefore making the flat bottom the most efficient for  $Q_f$ . On the other hand, the shear in the remote case is shielded from the bottom by an initially quiescent layer, which means the effect of bottom friction is weaker. This could prove useful in determining parameterizations of flux and diffusivity based on the depth of the current

With increased slope, the diffusivity curve and heat flux curves no longer match. This is illustrated quite clearly in the 3300-meter  $K_T$  and  $Q_f$  where the interpolated optimal slope for  $K_T$  is of smaller value than that for  $Q_f$ . Similarly, the orientation cases show a maximum angle for  $Q_f$  that is not the same orientation angle as those with maximum  $K_T$ . In cases of extreme slope or orientation, heat flux and diffusivities are no longer proportional. This result is significant in that it justifies making model comparisons using multiple diagnostics.

In the orientation cases, the thermal gradient is shifted along with the flow to where it runs east—west and south—north with the same applied Coriolis force, effectively changing the realm of what we see on earth. With the Coriolis force being weaker at the equator, one might expect that the reason for this intense  $Q_f$  in our  $\Theta=180^\circ$  model is due to our horizontal thermal gradient. If we look at this in terms of what would happen if warmer water were to the north vice the equator, and neglected any changes in atmospheric dynamics that would occur from this, we would have a thermal/density gradient and Coriolis gradient running parallel. Unlike in nature where the warmest water temperatures occur where there is the least Coriolis force, orientations above  $120^\circ$  have a stronger Coriolis is in the same region as the warmer water. Perhaps this scenario generates more eddy motion / mixing in the north than what we observe near the equator. This may act as a “heat engine” that, along with thermal wind, promotes larger amounts of CFF. Perhaps in the future research is needed to validate this concept.

For the GRB model, the results illustrate that the assumptions built into this quasi-geostrophic formulation of the GRB model only capture very approximate qualitative behavior. The 3300 m 3-D model optimal slope falls in line with comparisons done between the basic two-layer QG model, as seen in Appendix A (Figure 20). However, the QG slope and magnitude are still half that of the 3-D scenario. This reaffirms that bottom slope does affect BI and that two-layer and analytic models may lack the ability to properly account for meridional-sloped topography.



## VI. RECOMMENDATIONS

There is a broad range of possible studies that can be done to continue this research as many other practical comparisons could be made. For example, changing the strength of shear, or comparing heat flux and diffusivities at different slopes to see when they match and when they begin to diverge. Below is a short summary of topics that one may wish to explore, but there are many other possibilities that would undoubtedly be directly relevant to oceanography and geophysical fluid dynamics.

1. The effects of mesoscale and sub-mesoscale bottom features on meridional transport: This study could use the same numeric model setup but create one or many bottom features replicating underwater mountains or atolls with scales from 10 to 100 km and heights extending through a significant fraction of water depth. A comparison could then be made between the total meridional heat and PV flux with and without these features and according to their size and comparing them to the uniform slope data in this paper.

2. Examining the effects of different shear patterns to determine what shear characteristic plays the dominant role in the dynamics of BI. This can be accomplished by varying the speed of the surface current and thus changing the gradient of the flow over depth, and by introducing various shears in different water depths.

3. Continued work on the orientation cases to improve our understanding of physical processes controlling the variability of heat transport with the flow direction.

4. Determining the effect of eddies in remote and direct case on sea surface height and temperature to determine and correct systematic errors in satellite bathymetry calculations. This experiment can be initiated by attempting to recreate a height-varying topography on the model seafloor from the sea surface data of the ocean using the model output data post-equilibrium.

THIS PAGE INTENTIONALLY LEFT BLANK

## APPENDIX A. COMPLEMENTARY FIGURES

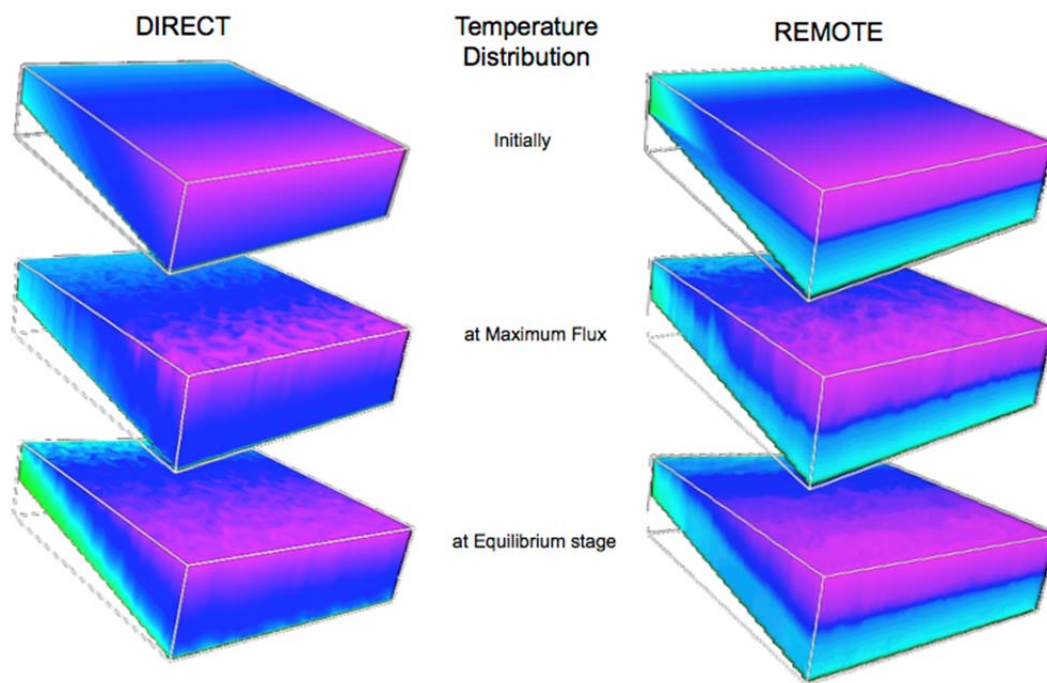


Figure 18. 3-D Captures of 1100-meter Direct and Remote Model Runs

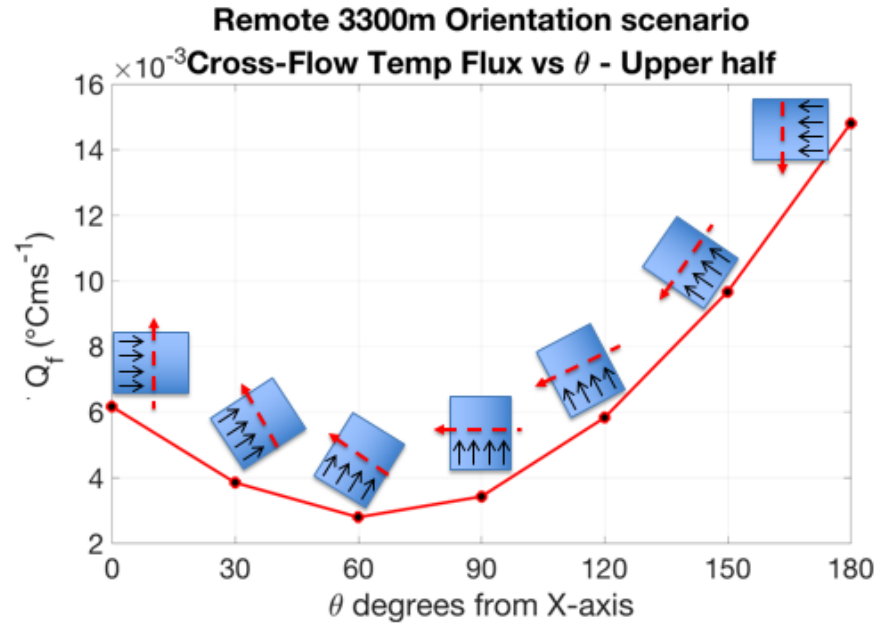


Figure 19. Orientation CFF with Orientation Diagram for Visual Reference

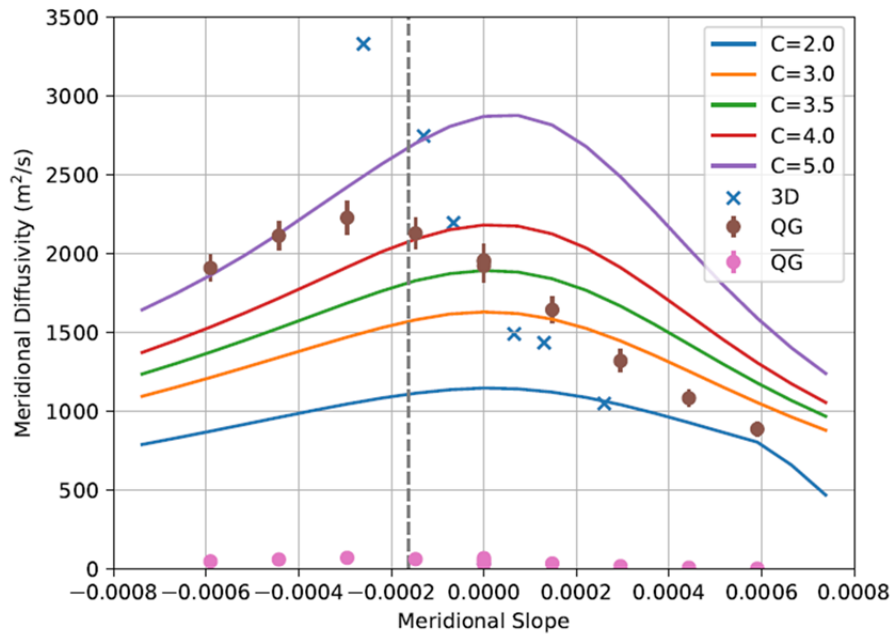


Figure 20. GRB with 3-D 3300-meter and Quasi-Geostrophic Comparison

## APPENDIX B. DATA TABLE

Below is the data collected from various model runs. Orient\_ represents the orientation runs, 3D\_ represents the 1100 m zonal flow remote case, and 8D\_ represents the 3300 m zonal flow remote case.

JOB	Depth	slope	theta	Qf	Qf MITgcm	KT
orient30N	3300	0	30	6.164E-03	6.155E-03	1.740E+03
orient60N	3300	0	60	3.847E-03	1.197E-02	2.074E+03
orient90N	3300	0	90	2.794E-03	1.897E-02	3.549E+03
orient120N	3300	0	120	3.424E-03	1.960E-02	9.046E+03
orient150N	3300	0	150	5.827E-03	1.897E-02	1.155E+04
orient180	3300	0	180	9.665E-03	1.611E-02	1.140E+04
3D_SN_RL_5	1100	-2.600E-04	0	6.637E-03	6.715E-03	1.762E+03
3D_SN_RL_25	1100	-1.300E-04	0	7.486E-03	7.440E-03	2.135E+03
3D_SN_RL_125	1100	-6.550E-05	0	8.104E-03	8.030E-03	2.282E+03
3D_RL_FB	1100	0.000E+00	0	5.422E-03	5.516E-03	1.468E+03
3D_NS_RL_125	1100	6.550E-05	0	4.231E-03	4.185E-03	1.065E+03
3D_NS_RL_25	1100	1.300E-04	0	3.148E-03	3.110E-03	7.610E+02
3D_NS_RL_5	1100	2.600E-04	0	2.059E-03	1.998E-03	4.766E+02
8D_SN_RL100	3300	-5.244E-04	0	1.075E-02	1.078E-02	3.507E+03
8D_SN_RL_75	3300	-3.933E-04	0	1.061E-02	1.056E-02	3.521E+03
8D_SN_RL_5	3300	-2.600E-04	0	1.023E-02	1.013E-02	3.328E+03
8D_SN_RL_25	3300	-1.300E-04	0	9.067E-03	9.148E-03	2.791E+03
8_SN_RL_125	3300	-6.550E-05	0	7.438E-03	7.340E-03	2.194E+03
8D_RL_FB	3300	0.000E+00	0	6.164E-03	6.155E-03	1.740E+03
8D_NS_RL_125	3300	6.550E-05	0	5.483E-03	5.462E-03	1.491E+03
8D_NS_RL_25	3300	1.300E-04	0	5.347E-03	5.316E-03	1.435E+03
8D_NS_RL_5	3300	2.600E-04	0	4.091E-03	4.059E-03	1.050E+03

THIS PAGE INTENTIONALLY LEFT BLANK

## LIST OF REFERENCES

- Charney J.G., and Flierl, G.R., 1981: Oceanic analogues of large-scale atmospheric motion. *Evolution of Phys. Oceanogr.* B. A. Warren and C. Wunsch, Eds, The MIT Press, 504–549.
- Chen, C., and Kamenkovich, I., 2013: Effects of topography on baroclinic instability. *J. Phys. Oceanogr.*, **40**, 790–804.
- Church, P. E., 1932: Progress in the investigation of surface-temperatures of the Western North Atlantic. *Transactions, Am. Geophys. Union*, **13**, 244–249.  
<https://doi.org/10.1029/tr013i001p00244>.
- Church, P. E. 1937: Temperatures of the Eastern North Atlantic from thermograph records. *Union Geod Geophys Int. Association d’Oceanographie Physique*, **4**, 3–40.
- Dewar, W. K., 1998: Topography and barotropic transport control by bottom friction. *J. of Marine Res.*, **56**, 295–328, <https://doi.org/10.1357/002224098321822320>.
- Eady, E. T., 1949: Long waves and cyclone waves. *Tellus*, **1**, 33–52.  
<https://doi.org/10.1111/j.2153-3490.1949.tb01265.x>.
- Gent, P. R., and J. C. McWilliams, 1990: Isopycnal mixing in ocean circulation models. *J. Phys. Oceanogr.*, **20**, 150–155.
- Goff, J. A., and Arbic, B. K., 2010: Global prediction of abyssal hill roughness statistics for use in ocean models from digital maps of paleo-spreading rate, paleo-ridge orientation, and sediment thickness. *Ocean Modelling*, **32**, 36–43.  
<https://doi.org/10.1016/j.ocemod.2009.10.001>
- Green, J. S. A., 1970: Transfer properties of the large-scale eddies and the general circulation of the atmosphere. *Quarterly J. of the Roy. Meteor. Soc.*, **96**, 157–185.  
<https://doi.org/10.1002/qj.49709640802>.
- Holloway, G., 1987: Systematic forcing of large-scale geophysical flows by eddy-topography interaction. *Journal of Fluid Mechanics*, **184**, 463.  
<https://doi.org/10.1017/s0022112087002970>.
- Iselin, C. O’D., 1936: A study of the circulation of the western North Atlantic. *Papers on Phys. Oceanography and Meteorology*, **IV(4)**, 101 pp.  
<https://doi.org/10.1575/1912/1087>.
- Kamenkovich, I., P. Berloff, and J. Pedlosky, 2009: Role of eddy forcing in the dynamics of multiple zonal jets in a model of the North Atlantic. *J. Phys. Oceanogr.*, **39**, 1361–1379.

- Kamenkovich, V. M., Koshlyakov, M. N., and Monin, A. S., 1986: Eddies in the open ocean. *Synoptic Eddies in the Ocean*, 265–376. [https://doi.org/10.1007/978-94-009-4502-9\\_5](https://doi.org/10.1007/978-94-009-4502-9_5)
- Knauss, J. A., 2000: *Introduction to Physical Oceanography*. 2nd. Prentice-Hall. 303 pp.
- Marshall, J., Hill, C., Perelman, L., and Adcroft, A. 1997: Hydrostatic, quasi-hydrostatic, and nonhydrostatic ocean modeling. *Journal of Geophysical Research. Oceans*, **102**, 5733–5752. <https://doi.org/10.1029/96jc02776>.
- Maslowski, W., and Lipscomb, W. H., 2003: High resolution simulations of Arctic sea ice, 1979–1993. *Polar Res*, **22**, 67–74.
- McWilliams, J. C., 2011: *Fundamentals of Geophysical Fluid Dynamics*. Cambridge Univ. Press., 249 pp.
- Menemenlis, D., Fukumori, I., and Lee, T., 2005: Using Green's functions to calibrate an ocean general circulation model. *Monthly Weather Review*, **133**, 1224–1240. <https://doi.org/10.1175/mwr2912.1>.
- NASA Goddard Space Flight Center, 2011: *Perpetual Ocean*. 29 December 2016, <http://svs.gsfc.nasa.gov/3827>.
- Phillips, N. A., 1951: A simple three-dimensional model for the study of large-scale extratropical flow patterns. *J. Meteor.*, **8**, 381–394.
- Radko, T., De Carvalho, D. P., Flanagan, J., 2014: Nonlinear equilibration of baroclinic instability: The Growth Rate Balance model. *J. Phys. Oceanogr.* **44**, 1919–1940. <https://doi.org/10.1175/jpo-d-13-0248.1>.
- Robinson, A. R., 1983: *Eddies in Marine Science*. Springer-Verlag, 609 pp
- Polzin, K. L., Toole, J.M., Ledwell, J.R., and Schmitt, R.W., 1997. Spatial variability of turbulent mixing in the abyssal ocean. *Science*, **276**, 93–96. <https://doi.org/10.1126/science.276.5309.93>.
- Spall, M. A. and D. C. Chapman, 1998: On the efficiency of baroclinic eddy heat transport across narrow fronts. *J. Phys. Oceanogr.*, **28**, 2275–2287.
- Steiner, N., Holloway, G., Gerdes, R., Häkkinen, S., Holland, D., and Karcher, M., 2004: Comparing modeled streamfunction, heat and freshwater content in the Arctic Ocean. *Ocean Modelling*, **6**, 265–284. [https://doi.org/10.1016/s1463-5003\(03\)00013-1](https://doi.org/10.1016/s1463-5003(03)00013-1).
- Sutyrin, G. G., and Grimshaw, R., 2005: Frictional effects on the deep-flow feedback on the -drift of a baroclinic vortex over sloping topography. *Deep Sea Research Part I: Oceanographic Res. Papers*, **52**, 2156–2167. <https://doi.org/10.1016/j.dsr.2005.06.017>.



- Sutyrin, G. G., and Grimshaw, R., 2010: The long-time interaction of an eddy with shelf topography. *Ocean Modelling*, **32**, 25–35.  
<https://doi.org/10.1016/j.ocemod.2009.08.001>.
- Thompson, A. F., 2010: Jet formation and evolution in baroclinic turbulence with simple topography. *J. Phys. Oceanogr.*, **40**, 257–278.
- Visbeck, M., J. Marshall, and T. Haine, 1997: Specification of eddy transfer coefficients in coarse-resolution ocean circulation models. *J. Phys. Oceanogr.*, **27**, 381–402.
- Williams, J. 1793: Memoir of Jonathan Williams on the use of the thermometer in discovering banks, soundings, etc., *Transactions of the American Philosophical Society*, **3**, 82–100.

THIS PAGE INTENTIONALLY LEFT BLANK

## **INITIAL DISTRIBUTION LIST**

1. Defense Technical Information Center  
Ft. Belvoir, Virginia
2. Dudley Knox Library  
Naval Postgraduate School  
Monterey, California